The Astronomical Journal, 154:2 (9pp), 2017 July https://doi.org/10.3847/1538-3881/aa72db

Estimating Jupiter's Gravity Field Using *Juno* Measurements, Trajectory Estimation Analysis, and a Flow Model Optimization

Eli Galanti[1], Daniele Durante[2], Stefano Finocchiaro[2,3], Luciano Iess[2], and Yohai Kaspi[1]
[1] Department of Earth and Planetary Sciences, Weizmann Institute of Science, Rehovot, Israel; eli.galanti@weizmann.ac.il
[2] Dipartimento di Ingegneria Meccanica e Aerospaziale, Sapienza Universita di Roma, Rome, Italy
Received 2016 December 25; revised 2017 March 30; accepted 2017 May 10; published 2017 June 8

Abstract

The upcoming *Juno* spacecraft measurements have the potential of improving our knowledge of Jupiter's gravity field. The analysis of the *Juno* Doppler data will provide a very accurate reconstruction of spatial gravity variations, but these measurements will be very accurate only over a limited latitudinal range. In order to deduce the full gravity field of Jupiter, additional information needs to be incorporated into the analysis, especially regarding the Jovian flow structure and its depth, which can influence the measured gravity field. In this study we propose a new iterative method for the estimation of the Jupiter gravity field, using a simulated *Juno* trajectory, a trajectory estimation model, and an adjoint-based inverse model for the flow dynamics. We test this method both for zonal harmonics only and with a full gravity field including tesseral harmonics. The results show that this method can fit some of the gravitational harmonics better to the "measured" harmonics, mainly because of the added information from the dynamical model, which includes the flow structure. Thus, it is suggested that the method presented here has the potential of improving the accuracy of the expected gravity harmonics estimated from the *Juno* and *Cassini* radio science experiments.

Key words: gravitation – hydrodynamics – planets and satellites: gaseous planets – planets and satellites: individual (Jupiter, Saturn)

1. Introduction

The Jovian gravity field is determined by means of accurate measurements of a spacecraft range rate. The observable quantities are processed by an orbit determination code, which estimates the gravity harmonic coefficients together with the spacecraft state and other parameters of the model. These estimates of the gravity field, which by themselves rely on modeling of the observables, may be aided and improved when geophysical models are incorporated in this analysis.

The potential for a new estimate of Jupiter's gravity field comes from the NASA *Juno* spacecraft that currently is in orbit around Jupiter. One of the scientific goals of the *Juno* mission is the accurate determination of the gravity field of the planet (Bolton 2005). The gravity experiment is based on the measurement of the Doppler shift in a coherent two-way radio link, consisting of a ground station transmitting a reference signal that is received by a transponder on *Juno* and retransmitted back to Earth preserving phase coherence. The same ground station receives the downlink signal and measures its Doppler shift by comparing the incoming and outgoing signals. *Juno*'s Doppler observables are especially accurate thanks to the use of a Ka-band radio link at 32–34 GHz. Indeed, at these frequencies the noise from interplanetary plasma is strongly reduced. *Juno*'s radio science system enables range rate measurements accurate to 3×10^{-6} m s^{-1} over timescales of 1000 s.

The Doppler shift is processed by an orbit determination code to provide very accurate information on Jupiter's gravity field. The orbit determination analysis relies on two main background gravity measurements. The first is a previously estimated value of Jupiter's gravity field (Jacobson 2003), which provides a first indication of the solid-body contribution. A second source of spatially and time-dependent gravity variation is related to Jupiter normal modes, which may perturb the gravity field to a considerable level (Durante et al. 2016).

The deviation of Jupiter's gravity field from that of a point mass may result from two main sources. The first is the deviation of the planet from sphericity as a result of its rotation (e.g., Hubbard 1984). An oblate planet results in a gravity field that depends on latitude with symmetry between the northern and southern hemispheres. This latitudinal dependence also depends on the planet's internal density distribution. Lack of knowledge on the density distribution inside Jupiter results in large uncertainties regarding the planet solid-body gravity field (e.g., Hubbard & Militzer 2016; Miguel et al. 2016; Wahl et al. 2017).

The second source of spatially dependent gravity variations is the existence of differential flow (deviations with respect to the mean solid-body rotation) within the planet. Such flow would be accompanied by redistribution of the density field (e.g., Kaspi et al. 2010) and therefore will have an impact on the gravity field. Knowledge about the shape and density distribution of the solid body could help to determine the low-degree even gravity harmonics (mostly J_2, J_4, J_6 and J_8), while knowledge about the differential flow dynamics should improve the estimate of the low-degree odd harmonics J_3, J_5 and J_7 and the gravity harmonics higher than J_8.

Several studies discussed the relation between Jupiter-observed cloud-level wind and the gravity field induced by the wind (e.g., Hubbard 1999; Kaspi et al. 2010, 2016; Kaspi 2013; Zhang et al. 2015). Some assume cylindrically symmetric flow, while others allow for the wind to decay with depth. Other studies demonstrated that regardless of the depth of the cloud-level flow, a wind-density relation that is based on thermal wind balance is valid for Jupiter (Kaspi et al. 2016; Galanti et al. 2017). Recent studies investigated the inverse problem of deducing the flow structure from the measured

---

[3] Now at Arpsoft, Rome, Italy.

gravity field (Galanti & Kaspi 2016, 2017) and showed that under reasonable physical assumptions, the flow field could be derived from the expected *Juno* observations with an uncertainty on the depth of the flow that is at least an order of magnitude smaller than the value itself.

Here we propose a novel approach to improve the gravity field estimate by including in the analysis the estimation of Jupiter's flow field. An improved estimate of the Jupiter gravity field is accomplished using an iterative method based on simulated *Juno* measurements, a trajectory estimation model (TEM), and an adjoint-based inverse flow model (FM). We show that the method can lead to improved gravity analysis under completely different scenarios that might be expected on Jupiter. The inclusion of an inverse model for the solid-body solution should in principle improve the gravity estimate even further, but this task is beyond the scope of this study.

The manuscript is organized as follows: in Section 2 we present the two models used in the study—the TEM and the FM. In Section 3 we discuss the experimental setup, and the results are presented in Section 4. A discussion and conclusion is given in Section 5.

2. Models

The method used in this study is comprised by two completely independent methods for calculating the Jupiter gravitational harmonics. The TEM uses the observed *Juno* range rate to estimate the gravity harmonics, and the FM uses the observed cloud-level wind to calculate the wind-induced gravity harmonics. Below we discuss the two methods and the experimental setup that combines them to obtain an optimized solution.

2.1. The Trajectory Estimation Model (TEM)

The trajectory estimation process estimates a set of parameters that affect the spacecraft motion. The recovery of the spacecraft trajectory is obtained through reconstructing the acceleration acting on the spacecraft, which mainly depends on, but is not limited to, the gravity field coefficients. Thus, the estimation of the spacecraft trajectory encompasses an estimate of the Jupiter gravity field in terms of spherical harmonic coefficients.

The accelerations acting on the spacecraft can be summarized as

$$\boldsymbol{g}_{\mathrm{all}} = -\nabla U + \boldsymbol{g}_{\mathrm{N}} G.$$

Here, $\boldsymbol{g}_{\mathrm{N}} G$ includes the non-gravitational acceleration. The variable U is the gravitational potential of the planet, which is expanded in spherical harmonics

$$U(r,\theta,\phi) = -\frac{GM}{r}\left\{1 + \sum_{l=2}^{\infty}\left(\frac{a}{r}\right)^{l}\sum_{m=0}^{\infty} C_{l,m}P_{l,m}(\mu)\cos(m\phi) + \sum_{l=2}^{\infty}\left(\frac{a}{r}\right)^{l}\sum_{m=0}^{\infty} S_{l,m}P_{l,m}(\mu)\sin(m\phi)\right\}, \qquad (1)$$

where G is the gravitational constant, M is the Jupiter mass, a is the planet mean radius, $P_{l,m}$ are the un-normalized associated Legendre polynomials, $C_{l,m}$, $S_{l,m}$ are the spherical harmonics coefficients to be calculated, and $\mu = \cos\theta$, with θ being the latitude.

The dynamical model of the spacecraft, discussed extensively by Finocchiaro & Iess (2010), Finocchiaro (2013), and Tommei et al. (2015), accounts for gravitational accelerations from all solar system bodies and from the Galilean satellites, as well as for the tides raised by the satellites on Jupiter. The non-gravitational accelerations include the effect of the solar radiation pressure on *Juno*'s large solar panels, the Jupiter albedo, and thermal emission. The Lense-Thirring effect, although inseparable from an offset of Jupiter's pole (Le Maistre et al. 2016), is included as a deterministic known effect. The Jupiter rotation model is based on the IAU convention (Archinal et al. 2011). The possible effects of Jupiter normal modes on its gravitational field (Durante et al. 2016) and thus on the proposed optimization method are not accounted for.

The simulation of the *Juno* gravity experiments (see discussion of experimental setup in Section 3) is carried out with JPL's newest orbit determination code (MONTE, see Evans et al. 2016) and a separate, multi-arc weighted least-squares differential corrector for the estimation process. The synthetic Doppler data for a two-way Ka-band radio link is simulated for all perijove arcs devoted to gravity science, on the reference 14-day trajectory for the *Juno* orbital phase.[4] Each arc is 24 hr long, centered on the closest Jupiter approach (see Figure 1, where the tracks are shown for −20 to +20 minutes around perijove), and include approximately an 8 hr long tracking arc, according to the relative geometry of *Juno* and NASA's DSS 25 at NASA's DSN Goldstone complex, the only station capable of transmitting in Ka-band. White noise with a standard deviation of 0.020 mm s^{-1} is added to the observable at 60 s to simulate realistic Doppler data points. Note that *Cassini* Ka/Ka two-way coherent radio link data points collected during cruise phase show a noise on Doppler data as low as 0.012 mm s^{-1} at 60 s (Asmar et al. 2005). The level of noise selected in this study also accounts for variability with tracking conditions, thus is larger than the best performances achievable with current radio tracking systems.

The estimation process iteratively converges to the solution by computing differential corrections starting from a reference solution. The parameters to be solved include the *Juno* initial condition for each arc, the gravitational coefficients $C_{l,m}$, $S_{l,m}$ (in principle, up to arbitrary degree and order), the Love numbers k_2, k_3, and k_4, and the Jupiter pole direction, R.A. and decl. in the EME2000 frame, and their rates (Archinal et al. 2011).

The partial derivatives of the frequency residual of Doppler observables with respect to the parameter list are computed,

$$y_i = f^{\mathrm{observed}} - f^{\mathrm{computed}}, \qquad (2)$$

$$\boldsymbol{H}_i = \frac{\partial y_i}{\partial \boldsymbol{x}},\ for\ i = 1,\ldots,N, \qquad (3)$$

where $\boldsymbol{x}$ are the estimated parameter set at the reference epoch, $\boldsymbol{y}$ are the Doppler observables residuals y_i, $\boldsymbol{H}_i$ is a vector containing the partial derivatives of a Doppler point with respect to the unknown parameters $\boldsymbol{x}$, to be collected in the

---

[4] Because of concerns about the performances of the propulsion system, *Juno* is currently on a 53-day orbit. It is currently unknown if and when *Juno* could attain its originally planned orbit. The conclusions of this study are largely independent of the orbital period.

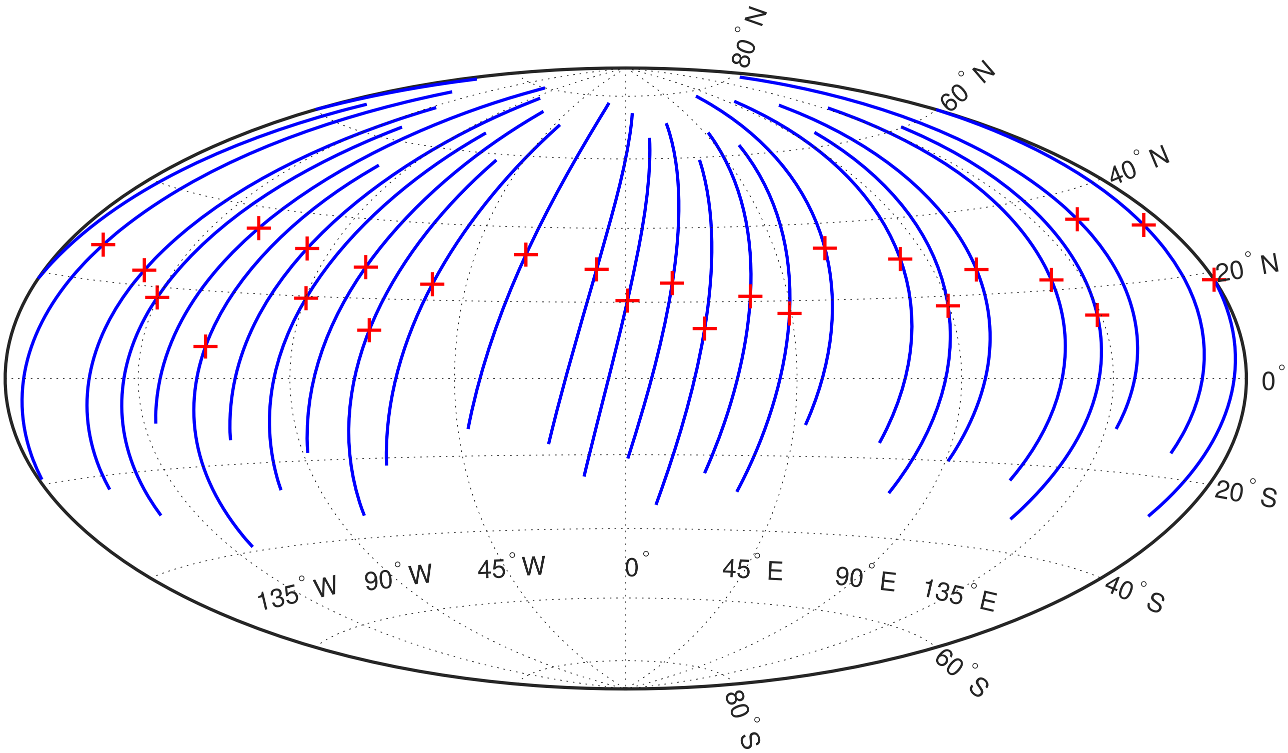

Figure 1. *Juno* gravity tracks shown on a global map of Jupiter. Lines indicate the location of the track from 20 minutes before perijove to 20 minutes after. The location of the perijove for each track is marked with a red cross.

matrix $\boldsymbol{H}$ (with a size given by the number of observables times the number of unknown parameters), and N is the number of Doppler points. The least-squares filter provides the differential correction on the parameters

$$\delta\boldsymbol{x}_k = (\boldsymbol{H}^T\boldsymbol{W}_H\boldsymbol{H} + \bar{\boldsymbol{P}}_k^{-1})^{-1}(\boldsymbol{H}^T\boldsymbol{W}_H\boldsymbol{y} + \bar{\boldsymbol{P}}^{-1}\bar{\boldsymbol{x}}_k), \tag{4}$$

with the covariance matrix given by

$$\boldsymbol{P} = (\boldsymbol{H}^T\boldsymbol{W}_H\boldsymbol{H} + \bar{\boldsymbol{P}}^{-1}), \tag{5}$$

where $\boldsymbol{W}_H$ is a diagonal weight matrix for the Doppler residuals, $\bar{\boldsymbol{P}}$ is the a priori covariance matrix for the parameters, and $\bar{\boldsymbol{x}}_k$ is the difference between the reference solution and the current estimated value, at kth iteration (starting from $\bar{\boldsymbol{x}}_0 = 0$). See Tapley et al. (2004) for further details on the orbit determination process. The process is iterated until convergence is attained, i.e., until the frequency residuals appear unbiased and consistent with the expected spectral properties of the noise. The SRIF filter provides the estimated parameters and their covariance matrix, allowing the process to converge. When the residuals are fitted to the noise level, a statistically trustable trajectory is recovered and an estimate of the gravity field harmonic coefficients is retrieved.

2.2. The Flow Model (FM)

Two versions of the FM are used in this study. The first is solving the gravitational field based on the zonally symmetric wind (Galanti & Kaspi 2016), while the second solves the case where both the zonal and meridional cloud-level winds are assumed to affect the density field (Parisi et al. 2016).

In both versions, the cloud-level wind is based on the analysis of *Cassini* images (Choi & Showman 2011), in which both the zonal and meridional velocities are estimated as a function of longitude and latitude. The spatial variability of the cloud-level wind is illustrated in Figure 2, where the strong equatorial zonal flow is apparent as well as the location of the Great Red Spot around 20°S and 90°W (a more detailed and quantitative analysis is given in Parisi et al. 2016).

The observed cloud-level winds are then projected inward along lines parallel to the axis of rotation, and are assumed to decay toward the planet center using a global radial decay depth, so that the 3D flow field follows

$$u(r, \theta, \phi) = u_0(\theta, \phi)\exp\left[-\frac{a-r}{h_u}\right],$$
$$v(r, \theta, \phi) = v_0(\theta, \phi)\exp\left[-\frac{a-r}{h_u}\right], \tag{6}$$

where $u_0(\theta, \phi)$, $v_0(\theta, \phi)$ are the azimuthal and meridional components of the observed cloud-level wind (Choi & Showman 2011), and h_u is the decay scale of the cloud-level wind. Note that in the first version of the model, we set $v_0 = 0$ and average the zonal velocity over longitude so that $u_0 = u_0(\theta)$.

The 3D flow is then related to the density anomalies using the thermal wind balance

$$(2\boldsymbol{\Omega} \cdot \boldsymbol{\nabla})[\tilde{\rho}\boldsymbol{u}] = \nabla\rho' \times \boldsymbol{g}_0, \tag{7}$$

where $\boldsymbol{\Omega}$ is the planetary rotation rate, $\tilde{\rho}(r)$ is the background density field, $\boldsymbol{u}(\boldsymbol{r})$ is the 3D velocity, $\boldsymbol{g}_0(r)$ is the mean gravity vector, and $\rho'(r, \theta, \phi)$ is the dynamical density anomaly (Pedlosky 1987; Kaspi et al. 2009). Note that this version of thermal wind balance is difference than that common in Earth dynamics since here the meridional density gradients are balanced by the shear in the direction of the spin axis. Galanti

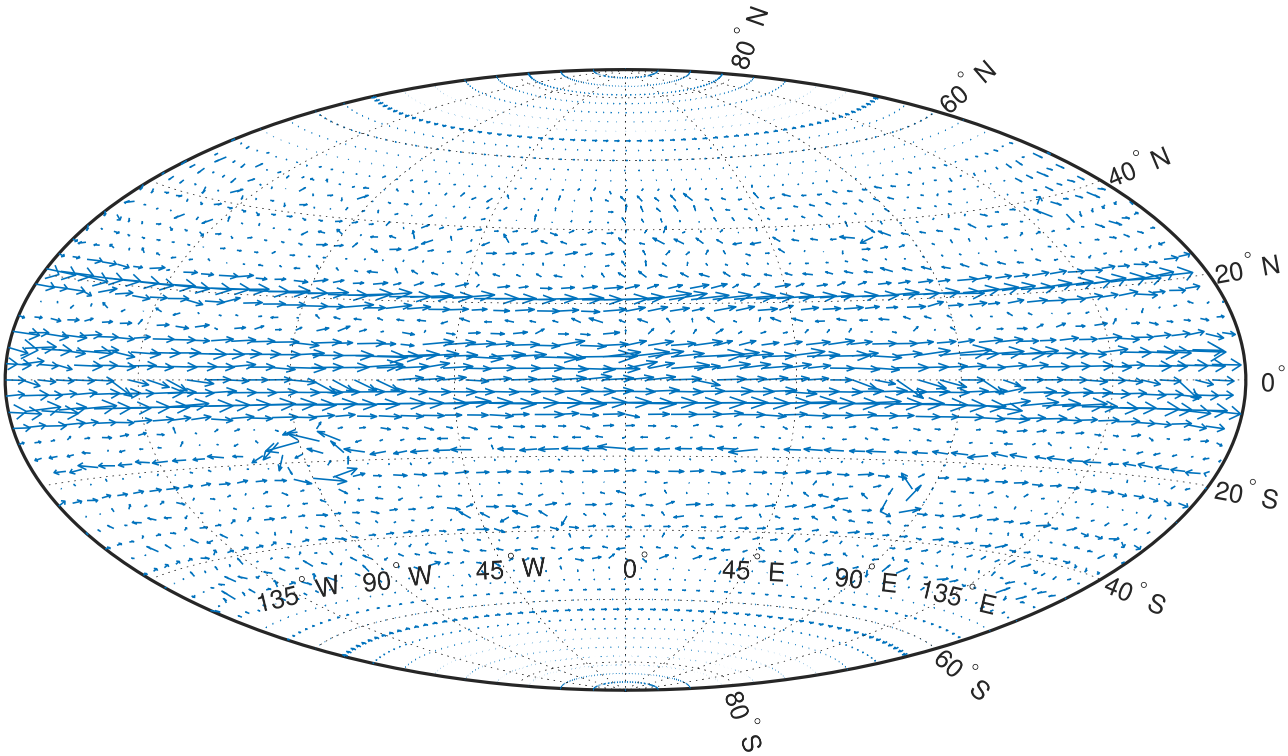

Figure 2. Observed cloud-level wind (Choi & Showman 2011). Shown are the wind vectors $[u_0, v_0]$ with a resolution of 3° in latitude and 6° in longitude. Arrow lengths correspond to the magnitude of the wind.

et al. (2017) have shown that deviations from thermal wind balance that are due to the effects of oblateness are small and have a negligible effect on the gravity harmonics. In the first setup (zonally symmetric), the 3D density field is degenerated in the longitude direction. From the density field the gravity harmonics are calculated. The zonal coefficients are

$$J_l = -\frac{2\pi}{Ma^l}\int_0^a r^{l+2}dr\int_{\mu=-1}^{1} P_{l,m=0}(\mu)\rho' d\mu, \qquad (8)$$

where $l \geqslant 2$ is the harmonic degree. The tesseral coefficients are

$$C_{lm} = \frac{1}{Ma^l}\frac{2(l-m)!}{(l+m)!}\int_{r=0}^{a} r^{l+2}dr \times \int_{\phi=0}^{2\pi}\int_{\mu=-1}^{1} P_{lm}(\mu)\cos(m\phi)\rho' d\mu d\phi, \qquad (9)$$

$$S_{lm} = -\frac{1}{Ma^l}\frac{2(l-m)!}{(l+m)!}\int_{r=0}^{a} r^{l+2}dr \times \int_{\phi=0}^{2\pi}\int_{\mu=-1}^{1} P_{lm}(\mu)\sin(m\phi)\rho' d\mu d\phi, \qquad (10)$$

where $l \geqslant 2$ and $m \geqslant 1$ are the degree and order of the expansion. Note that in the zonally symmetric case C_{lm} and S_{lm} are identically zero.

As discussed in Galanti & Kaspi (2016, 2017), the FM can be used in an optimization setup. Given a set of "measured" gravity harmonics $\boldsymbol{K}^0 = [J_l^o, C_{lm}^o, S_{lm}^o]$, the FM can be used to find the depth of the cloud-level winds h_u that results in a model solution $\boldsymbol{K}^m = [J_l^m, C_{lm}^m, S_{lm}^m]$ that minimizes the cost function

$$L = (\boldsymbol{K}^m - \boldsymbol{K}^o)\boldsymbol{W}_K(\boldsymbol{K}^m - \boldsymbol{K}^o)^T, \qquad (11)$$

where $\boldsymbol{W}_K$ is a weight matrix calculated as the inverse of the covariance matrix multiplied by 9 (equivalent to three times the uncertainties). Galanti & Kaspi (2017) explored complex scenarios in which the depth of the wind can vary with latitude, as well as scenarios in which in addition to the wind related to the cloud level, a deep flow exists that is completely separated. For the sake of simplicity, we assume here that there is no independent deep flow, and that the depth of the cloud-level wind is independent of latitude. When the *Juno* measurements are analyzed, these assumptions could be easily relaxed. Note also that since we are searching for one parameter only (depth of the wind), we do not use here the adjoint method in the optimization process (Galanti & Kaspi 2016, 2017). If a more complex scenario is desired, then the adjoint method will be needed in order to reduce the computational burden.

3. Experimental Setup

Since we do not know how deep the flow is on Jupiter, we examine here two distinctly different possible cases. Using the FM, we generate two potential scenarios, one in which the cloud-level winds are deep with a decay scale of $h_u = 3000$ km (Equation (6)), and another in which the winds are much shallower with a decay scale of $h_u = 300$ km. In the zonally symmetric setup, the zonal gravity harmonics (Equation (8)) are calculated up to the 50th degree (Figure 3, blue and red squares), while when using the full cloud-level winds, the tesseral field up to degree 30 is used (Equations (8)–(10)). Given these gravity harmonics, the TEM is used to integrate a *Juno* trajectory and the corresponding Doppler observables for two scenarios of flow.

The number of gravity harmonics to be used in the TEM is a balance between the expected magnitude of the measured

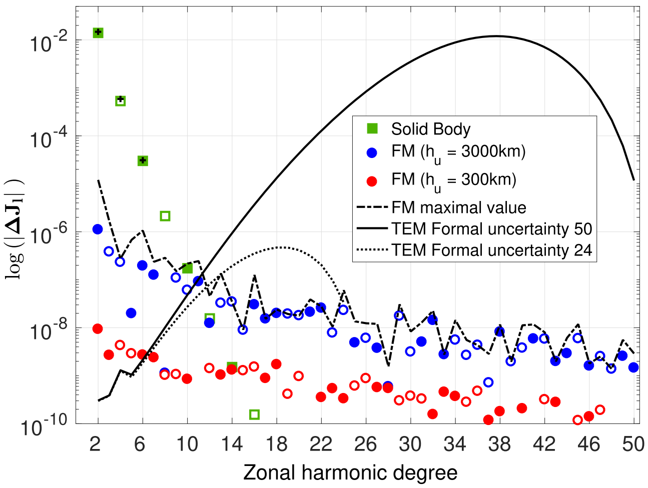

Figure 3. FM zonal gravity harmonics for the deep (blue) and shallow (red) wind cases, and maximum values (dashed black line). The solid and dotted lines show the formal uncertainties of the TEM, and the green squares indicate the solid-body harmonics.

harmonics and the uncertainties in the TEM. This is evident in Figure 3, where the solid and dotted black lines show the formal uncertainty associated with a TEM solution based on 50 and 24 zonal gravity harmonics, respectively. The decrease in uncertainty for higher degree harmonics is an artifact caused by the truncation of the estimated spherical harmonic coefficients. The former indicates that the maximum number of harmonics should not exceed 10 since the uncertainty in the higher harmonics is much higher than the expected values (dashed line). However, looking for a solution with only 10 harmonics will result in very large errors because higher degree contributions are neglected. We found that using 24 harmonics gives a good balance, and therefore we use this number of harmonics in the TEM throughout the experiments. This conclusion does not change when analyzing the full tesseral field (not shown), since the zonal coefficients J_l always have much higher values than the tesseral coefficients C_{lm}, S_{lm}.

The *Juno* orbit geometry (Figure 1) means that the low-degree harmonics are estimated in the TEM with a very good accuracy, while the uncertainty of the estimated higher harmonics increases rapidly (Figure 3, solid and dotted lines). It is possible to overcome this difficulty by associating an a priori covariance matrix with the estimated parameters (Tapley et al. 2004). This acts to constrain the solution and improve the numerical stability of the filter. We implement an a priori on gravity field coefficients (both zonal and tesseral field) according to the FM generated scenarios. Running the FM with different wind depths, the highest possible absolute value for each of the gravity harmonics is found (Figure 3, dash-dotted line). We use this upper limit multiplied by 10 as a priori for the TEM. This choice gives a physically based range where a solution could be searched for using the TEM. The scaling factor enables the filter to search in an even wider range of values than those predicted by the model, thus this choice does not provide a strict constraint.

Given the above choice of a priori information and the selected *Juno* trajectory scenario, the TEM is used to find a solution for the gravity harmonics. The solution, along with its accompanying error covariance matrix, is passed back to the FM as measurements and weights to be used in the cost function (Equation (11)). Since the TEM solves for the full gravity harmonics, which also include the unknown contribution from the solid-body rotation, we set to zero all the coefficients in the weight matrix W_K in Equation (11) that correspond to the even zonal gravity harmonics $l = 2, 4, 6, 8, 10$, so that these harmonics do not contribute to the cost function. As the $l > 10$ even zonal gravity harmonics from the solid-body rotation are much smaller than the corresponding harmonics from the atmospheric dynamics, they are retained in the minimization of the cost function. By optimizing the cost function, we find the wind depth h_u and its accompanying uncertainty (calculated from the Hessian matrix, see Galanti & Kaspi 2017). We also use the uncertainty in h_u to calculate the uncertainty in the solution for the gravity harmonics (see for details Galanti & Kaspi 2017). Finally, the TEM is used again to reestimate the gravity harmonics, but using the FM solution as an initial guess, and the uncertainty of the gravity solution from the FM (multiplied by 10) as an a priori. These back-and-forth iterations between the TEM and the FM are continued iteratively until the solution for the gravity field does not change beyond the a priori range associated with the TEM.

While in both the FM and TEM the calculation of the gravity field is made in spherical harmonics space, it is useful to analyze the outcome of the whole optimization process in terms of the physical gravity anomalies. This emphasizes the nature of the solutions and their uncertainties with respect to the locations of the *Juno* ground tracks. The gravity anomaly on the surface of a planet is defined as the difference between the calculated gravity acceleration and the reference gravity, composed of the point-mass gravity g_0 and accounting for contribution coming from the even zonal harmonics J_2, J_4, J_6, J_8, and J_{10}. These zonal harmonics are derived from a model of the interior structure. The resulting gravity anomalies in the radial direction are

$$\delta g_r(\mu, \phi) = -\frac{GM}{a^2}\sum_l (l+1) \times \sum_{m=0}^{l} P_{l,m}(\mu)[C_{l,m}\cos m\phi + S_{l,m}\sin m\phi], \quad (12)$$

with $l = 3, 5, 7, 9, 11, 12..., \infty$.

The overall process can be summarized as follows:

1. Use the FM solution, based on a prescribed flow pattern, to generate a simulation of the *Juno* trajectory (this stage will be replaced with the *Juno* observations).
2. Use the TEM to find the gravity harmonics, given an a priori based on the largest FM solution, and starting from a zero initial guess for the flow contribution.
3. Use the FM adjoint optimization to find the depth of wind whose induced gravity harmonics best match the TEM solution.
4. Use the TEM to find again the gravity harmonics, but now using the FM optimized solution as an initial guess, and an a priori based on the FM solution uncertainties.
5. Repeat stages 3 and 4 until the solution does not change beyond the a priori range associated with the TEM.

4. Results

Two main categories of experiments are conducted. In the first set of experiments (Section 4.1) we examine the method developed in this study assuming the flow on Jupiter

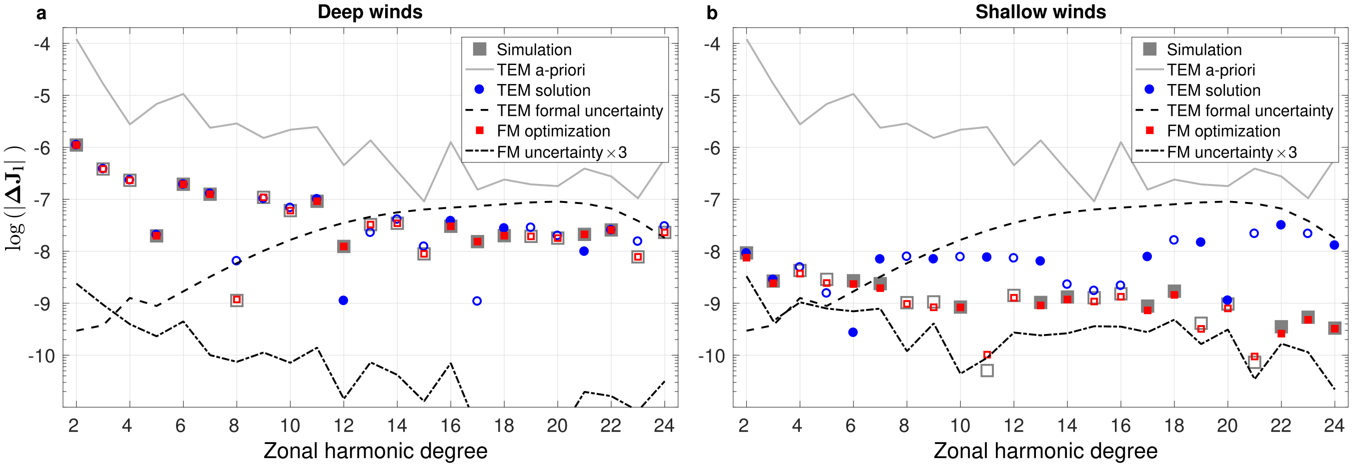

Figure 4. Two-step optimization process: first, given a general a priori (based on 10 times the FM maximal gravity field, see the dashed line in Figure 3), the TEM results in a gravity solution (blue squares), and its formal uncertainty (dashed line). Second, the FM is used to find an optimized solution (red squares), and the 3 times FM uncertainty (dash-dotted line). We also show for reference the simulations (gray squares). (a) Solutions for the deep wind case, (b) solutions for the shallow wind case.

is zonally symmetric. The second set of experiments is intended to simulate the measurements expected from *Juno*, therefore the full cloud-level wind is used and the full tesseral and zonal harmonics are computed (Section 4.2). In both categories we examine the cases of deep ($h_u = 3000$ km) and shallow flows ($h_u = 300$ km).

4.1. A Case with a Zonally Symmetric Flow

This experiment is meant to serve as a validation of the method presented in this study and to set a reference to the more realistic case discussed in Section 4.2. Using the FM, we generate a gravity field that is independent of longitude and conduct the entire iterative analysis using the zonal harmonics, both even and odd. The simulated measurements (Figure 3) are used to simulate the corresponding *Juno* trajectories. Then, the TEM is used to calculate the zonal gravity harmonics (Figure 4, blue squares), starting from the solid-body solution for J_2, J_4, J_6 and a zero initial guess for the rest of the coefficients, and using as a priori 10 times the FM maximum values (Figure 4, dotted line). We also show in Figure 4 the TEM uncertainties (dashed lines). Note that the TEM solutions are shown after subtracting the solid-body harmonics J_2, J_4, J_6, J_8 and J_{10}.

Next, the FM is used to fit the model solution to the TEM solution (Equation (11)) with weights based on 3 times the TEM uncertainties. The FM solution (Figure 4, red squares) is reached for $h_u = 3003 \pm 2$ km and $h_u = 281 \pm 11$ km for the deep and shallow winds, respectively. In both cases, the solution is within 2σ of the uncertainty, indicating that the process works well and is self-consistent. The FM ability to reach a good agreement with the TEM strongly depends on the uncertainty in the TEM. The effect of the TEM uncertainties on the solution in the TEM is substantial, especially for the higher coefficients, and it is much more pronounced in the shallow wind case. Thus the FM solution is in good agreement with the TEM whenever the gravity coefficient value is higher than the TEM uncertainty.

The question now is whether the optimized FM solution (Figure 4, red squares) can be used to help the TEM reach a better estimate of the gravity harmonics. In order to examine this, we run the TEM again, but this time using the solution of the FM as an initial guess, and using the uncertainties in gravity harmonics from the FM as a priori (Figure 4, dash-dotted lines) multiplied by 3. These uncertainties are very small, typically smaller than 10^{-9}, and therefore they greatly restrict the parameter space that needs to be searched by the least-squares filter of the TEM.

We find that in both cases the TEM can reach a new solution, as valid as the first solution, but much closer to the simulated measurements. The solution, which is within the TEM a priori, is reached after one iteration (additional iterations neither improve the solution nor cause it to diverge). In Figure 5 we show the gravity solution as function of latitude for the two cases. The simulated measurements (red) correspond to the blue and red squares in Figure 3. The blue lines are the TEM first solution, and the black lines are the TEM second optimized solution. For both TEM solutions, the accompanying uncertainties are shown as shading around the solutions. In both cases, the difference between the region where *Juno* is close to the perijove (see Figure 1) and the higher latitude regions is evident. The TEM has a much better ability to reach a good solution in the former case, while in the latter its errors and uncertainties are much larger, with a maximum near the south pole. It is also evident that the solution reached with the second optimized TEM setup is much better. The errors and the uncertainty (the black shading region is too small to be seen in the figure) are both much smaller, indicating a much better solution. It is also important to note the difference between the red line and the final black line. These differences essentially arise because even in the second stage, we compute the gravity signal only up to degree 24, whereas the red curve comes from a full FM solution up to degree 50.

4.2. A Case with the Full Latitude-longitude Flow

Next, we repeat the same procedure as we used in Section 4.1, but with a scenario in which the full wind field is used to generate the *Juno* trajectories. Again, we examine a case with deep winds and a case with shallow winds. Using the second version of the FM, we calculate a 30 by 30 tesseral field (Equations (9), (10)) with the density being derived from a 3D wind based on the observed cloud-level wind $[u_0(\theta, \phi), v_0(\theta, \phi)]$. The resulting gravity anomalies are shown as functions of latitude and longitude in Figures 6(a)

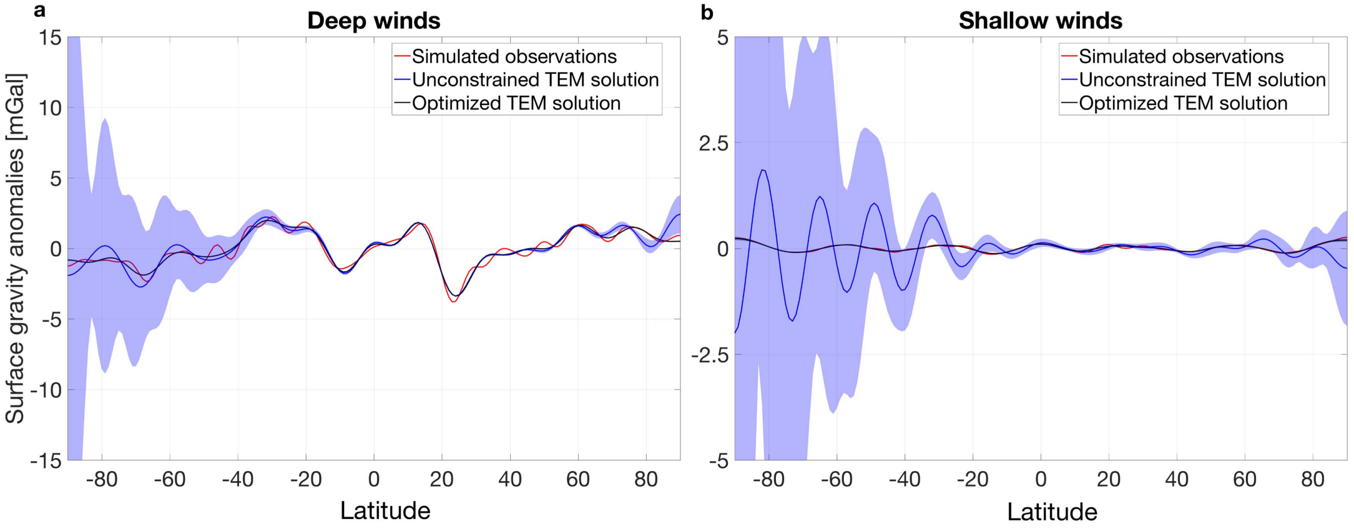

Figure 5. Wind-induced gravity anomalies as a function of latitude (Equation (12)). Shown are the simulated measurements (red), the first unconstrained TEM solution (blue), and the second optimized TEM solution (black). We also show the uncertainties associated with each solution (shadows). (a) Solutions for the deep wind case. (b) Solutions for the shallow wind case.

and (b) for the deep wind case and for the shallow wind case, respectively. While the dominant features remain longitude independent and similar to the zonally symmetric case, in some regions the deviations are substantial. For example, the location of the Great Red Spot can be clearly seen in both cases around 20°S and 90°W. It is a reflection of the anticyclonic vortex seen in Figure 2. Interestingly, in the deep wind case some regions in the northern hemisphere, around 90°W, also show strong gravity anomalies.

A gravity field that best explains the simulated *Juno* trajectory is then searched for using the TEM. Similar to the zonally mean experiments discussed in Section 4.1, as an a priori we use 10 times the maximum gravity harmonics calculated with the FM, and start from a zero initial guess for the non-solid-body gravity field. The first challenge is to determine the number of gravity harmonics to be used for each case. It is found that for the deep wind case, in addition to the 24 zonal coefficients, a field of 16 by 16 tesseral coefficients is required in order to reach a consistent solution. In the shallow wind case, a solution can be reached using only the zonal coefficients because the contributions coming from the zonally asymmetric flow are too small to be detected by TEM. The TEM solutions for the gravity field are shown in Figures 6(c) and (d). In the region where the *Juno* trajectory is close to the perijove (equatorial region and northward up to latitude 35), the gravity anomalies are close to the simulated measurements in both cases, similarly to the solutions in the zonally symmetric cases. However, the non-zonal features, such as the Great Red Spot, are not captured well in the deep wind case, and by definition, they are not captured at all in the shallow wind case (since only zonal coefficients are estimated). In the high latitudes, especially in the southern hemisphere, the solution differs greatly from the simulated measurements. The source of this behavior can be clearly seen in the uncertainties associated with the solutions (Figure 7), where the large uncertainty near the south pole dominates the map. In addition, the longitudes where larger uncertainties exists are also evident, especially around regions where the spacecraft does not pass.

Using the TEM solutions, the depth of the wind is found in the FM to be $h_u = 2999 \pm 2$ km and $h_u = 292 \pm 10$ km for the deep and shallow winds, respectively. When we again solve with the TEM using as an initial guess the FM solution as a priori and the uncertainties (multiplied by 3) associated with the FM gravity harmonics solution, an improved solution is reached (Figures 6(e) and (f)). Notably, the regions with the large errors seen in the first TEM solution now exhibit a much better agreement with the simulation. As in the previous experiments, one iteration is sufficient to reach a solution that is within the TEM uncertainties. Repeating the process results in a TEM solution that is almost identical to the solution shown here.

5. Discussion and Conclusions

The upcoming *Juno* orbits will enable an unprecedented high-accuracy estimate of the Jupiter gravity field with spatial variability. The analysis of the gravity field is expected to be spatially limited, however, because of the geometry of the *Juno* orbits, and additional physical knowledge about the expected gravity field may therefore help to improve the estimate.

Here we propose a new method for improving the *Juno* gravity analysis, usually obtained with a TEM, using the observed cloud-level wind and an inverse flow balance model that relates the flow on Jupiter to a resulting gravity field. The FM uses the observed cloud-level winds, projected inward to within the planet with a decay depth that can be adjusted (this could be easily modified to incorporate more complex flow structures, as discussed in Galanti & Kaspi 2016, 2017). The full 3D flow field is then related to density rearrangement via the thermal wind balance. We simulated two distinctly different flow regimes that might be expected to be measured by *Juno*. Using the FM, we generated two potential scenarios, one in which the cloud-level winds are deep with a decay scale of 3000 km (Equation (6)), and another in which the winds are much shallower with a decay scale of 300 km. Note that these two cases are used as an example, and other vertical structures can be used as well.

Beginning with the simulated gravitational field, the TEM together with an optimization procedure was used to obtain an initial solution for the gravitational harmonics. As an upper limit constraint (a priori), the TEM takes the gravity harmonics

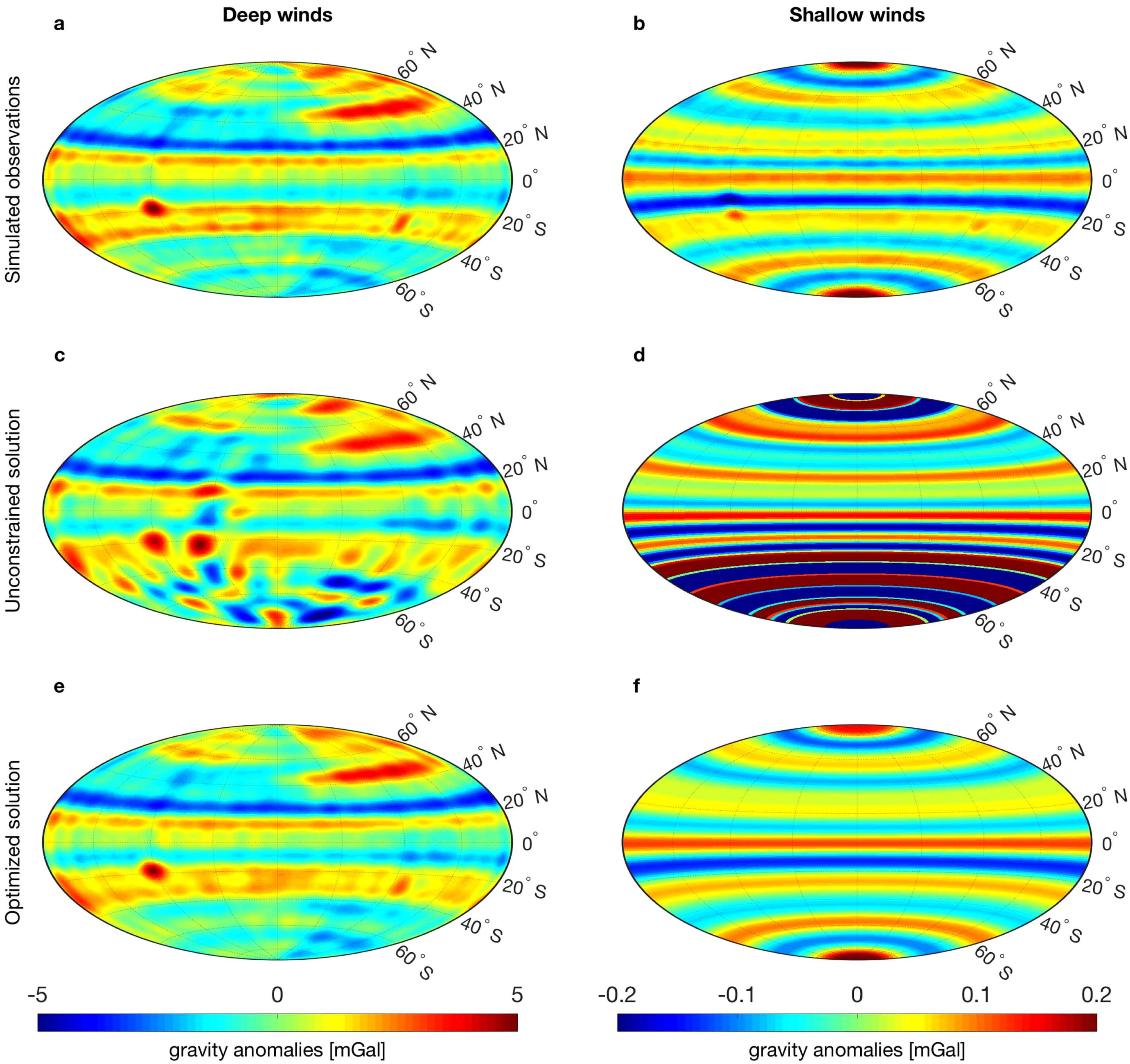

Figure 6. (a, b) Simulated measurements of the gravity anomalies δg_r in mGal. (c, d) The unconstrained TEM solution. (e, f) The optimized TEM solution. The left panels show solutions for the deep wind case. The right panels show solutions for the shallow winds case.

obtained from an FM in which the winds are assumed to penetrate barotropically along the direction of the spin axis. The solution from the TEM was then used as measurements for the FM, and together with an optimization method, the optimal penetration depth of the winds was computed and its uncertainty evaluated. As a final step, the gravity harmonics solution from the FM was returned to the TEM, along with an estimate of their uncertainties, to be used as an a priori for a new calculation of the gravity field. In all experiments done here, one exchange between the FM and the TEM was sufficient to reach a solution, but iterative repetition of this process might be required with the *Juno* observations.

We tested this method for several cases, with zonal harmonics only, and with the full gravity field including tesseral harmonics as well, related to the longitudinal variations of the wind profile. The results show that with this method, most of the gravitational harmonics are better fit to the "measured" harmonics, mainly because the FM takes the wind structure and depth into consideration. Thus, it is suggested that the method presented here has the potential of improving the accuracy of the expected gravity harmonics estimated through precise orbit determination of the *Juno* trajectory alone. A similar approach could be taken for the expected *Cassini* mission Grand Finale gravity measurements.

In this study we examined the effect of a wind-induced gravity signal on the gravity estimate. While this effect is important for estimating the low-degree odd harmonics J_3, J_5 and J_7 and the gravity harmonics higher than J_8, the low-degree even harmonics J_2, J_4, J_6 and J_8 are mostly affected by the

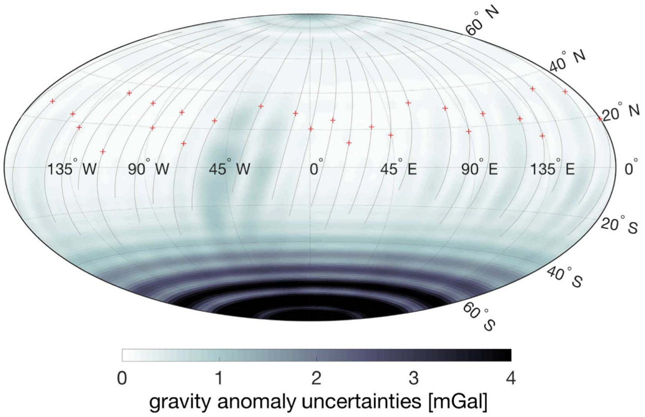

Figure 7. Uncertainties for the deep wind case. We also show the *Juno* trajectories (gray lines) and the locations of perijove for each pass (red crosses).

solid-body shape and density structure. In our experiments we assumed a known solution for the solid body (based on Hubbard 2012), but as recently discussed by Hubbard & Militzer (2016), there are large uncertainties associated with any solid-body solution for Jupiter. The inclusion of an inverse solid-body model should in principle improve the gravity estimate even further. This complex task is beyond the scope of this study and is left for future studies.

This research has been supported by the Israeli Ministry of Science and the Minerva foundation with funding from the Federal German Ministry of Education and Research. E.G. and Y.K. also acknowledge support from the Helen Kimmel Center for Planetary Science at the Weizmann Institute of Science. D.D., S.F., and L.I. have been supported in part by the Italian Space Agency.

References

Archinal, B. A., A'Hearn, M. F., Bowell, E., et al. 2011, CeMDA, 109, 101
Asmar, S. W., Armstrong, J. W., Iess, L., & Tortora, P. 2005, RaSc, 40, RS2001
Bolton, S. J. 2005, Juno Final Concept Study Report, Tech. Rep. AO-03-OSS-03, New Frontiers, NASA
Choi, D. S., & Showman, A. P. 2011, Icar, 216, 597
Durante, D., Guillot, T., & Iess, L. 2016, The Effect of Jupiter Oscillations on Juno Gravity Measurements, arXiv:1610.00250
Evans, S., Taber, W., Drain, T., et al. 2016, in VI Int. Conf. Astrodynamics Tools and Techniques (ICATT)
Finocchiaro, S. 2013, PhD thesis, Pubblicazioni Aperte Digitali della Sapienza, code 1889, Sapienza Universita di Roma
Finocchiaro, S., & Iess, L. 2010, in Spaceflight Mechanics, Vol. 136 (American Astronomical Society), 1417
Galanti, E., & Kaspi, Y. 2016, ApJ, 820, 91
Galanti, E., & Kaspi, Y. 2017, Icar, 286, 46
Galanti, E., Kaspi, Y., & Tziperman, E. 2017, JFM, 810, 175
Hubbard, W. B. 1984, Planetary interiors (New York: Van Nostrand Reinhold Co.)
Hubbard, W. B. 1999, Icar, 137, 357
Hubbard, W. B. 2012, ApJL, 756, L15
Hubbard, W. B., & Militzer, B. 2016, ApJ, 820, 80
Jacobson, R. A. 2003, JUP230 orbit solutions, http://ssd.jpl.nasa.gov/
Kaspi, Y. 2013, GeoRL, 40, 676
Kaspi, Y., Davighi, J. E., Galanti, E., & Hubbard, W. B. 2016, Icar, 276, 170
Kaspi, Y., Flierl, G. R., & Showman, A. P. 2009, Icar, 202, 525
Kaspi, Y., Hubbard, W. B., Showman, A. P., & Flierl, G. R. 2010, GeoRL, 37, L01204
Le Maistre, S., Folkner, W. M., Jacobson, R. A., & Serra, D. 2016, P&SS, 126, 78
Miguel, Y., Guillot, T., & Fayon, L. 2016, Jupiter Internal Structure: the Effect of Different Equations of State, arXiv:1609.05460
Parisi, M., Galanti, E., Finocchiaro, S., Iess, L., & Kaspi, Y. 2016, Icar, 267, 232
Pedlosky, J. 1987, Geophysical Fluid Dynamics, (Berlin: Springer)
Tapley, B. D., Bettadpur, S., Watkins, M., & Reigber, C. 2004, GeoRL, 31, 9607
Tommei, G., Dimare, L., Serra, D., & Milani, A. 2015, MNRAS, 446, 3089
Wahl, S. M., Hubbard, W. B., Militzer, B., et al. 2017, GeoRL, Vol. 44
Zhang, K., Kong, D., & Schubert, G. 2015, ApJ, 806, 270